UKAEA-CCFE-PR(21)59

Bin Zhu, Yiqiang Wang, Jiří Dluhoš, Andy J. London,
Michael Gorley, Mark J. Whiting, Tan Sui

# A novel pathway for multi-scale high-resolution time-resolved residual stress evaluation of laser-welded Eurofer97

# A novel pathway for multi-scale high-resolution time-resolved residual stress evaluation of laser-welded Eurofer97

Bin Zhu, Yiqiang Wang, Jiří Dluhoš, Andy J. London, Michael Gorley, Mark J. Whiting, Tan Sui

This is a preprint of a paper submitted for publication in Science Advances

Science Advances
Manuscript Template

FRONT MATTER

# A novel pathway for multi-scale high-resolution time-resolved residual stress evaluation of laser-welded Eurofer97

**Authors**

Bin Zhu[1], Yiqiang Wang[2], Jiří Dluhoš[3], Andy J. London[2], Michael Gorley[2], Mark J. Whiting[1], Tan Sui[1]*

**Affiliations**

[1] Department of Mechanical Engineering Sciences, University of Surrey, Guildford, Surrey, GU2 7XH, UK.

[2] United Kingdom Atomic Energy Authority, Culham Centre for Fusion Energy, Culham Science Centre, Abingdon, Oxon, OX14 3DB, UK.

[3] TESCAN ORSAY HOLDING, a.s., Libušina třída 21, 623 00 Brno, Czech Republic

* Corresponding author: t.sui@surrey.ac.uk;

**Abstract**

The plasma-facing components of future fusion reactors, where the Eurofer97 is the primary structural material, will be assembled by laser-welding techniques. The heterogeneous residual stress induced by welding can interact with the microstructure, resulting in a degradation of mechanical properties and a reduction in joint lifetime. Here, a $Xe^{+}$ plasma focused ion beam, with digital image correlation (PFIB-DIC) and nanoindentation are used to reveal the mechanistic connection between residual stress, microstructure and micro-hardness. This study is the first to use the PFIB-DIC to evaluate the time-resolved multi-scale residual stress at length-scale of tens of micrometres for laser-welded Eurofer97. A non-equilibrium micro-scale residual stress is observed, which makes a significant contribution at the macroscopy scale. The micro-hardness is similar for the fusion zone and heat affected zone (HAZ), although the HAZ exhibits around ~30% tensile residual stress softening. The results provide insight into maintaining structural integrity for this critical engineering challenge.

**Teaser**

A novel insight into residual stresses at different length scales and their effects on mechanical properties.

## Introduction

Nuclear fusion is a potential substitute source of electricity production, to solve dependence on fossil fuels, reduce carbon emissions and to provide a major contribution to net zero targets. The in-vessel components in the fusion plant, such as pipes, breeding blanket and divertor cassette, have to ustilse complex materials systems, complicated joining techniques and maintenance processes to enable their function under extreme operating conditions (1, 2). Laser welding is a promising technique that is used extensively in a wide range of industries to overcome the intrinsic assembly and maintenance difficulties (*3*, *4*). Previous studies have demonstrated the feasibility of using remote laser tools to butt-weld in-vessel components (*3*, *5*, *6*).

Reduced-activation ferritic/martensitic (RAFM) steels, which are an evolution of high Cr Grade 91 steel, are widely used as structural materials in various in-vessel components for the DEMOnstration power plant (DEMO). Eurofer97, one of the RAFM steels, uses lower activation elements like tungsten, vanadium and tantalum in appropriate quantities. It is used as the European reference material for the EU-DEMO reactor because its excellent mechanical properties: creep life, fracture, strength and ductility (*7–9*). When joining Eurofer97 this process does, however, induce significant residual stresses, up to c.800 MPa, as a result of the non-uniform deformation caused by the thermal cycle and the martensite phase transformation which takes place after welding (10, 11).

The residual stress largely originates from strain misfit between different regions and is usually categorised into three types according to the length scale (*12*). Type I (macro-scale) residual stress is usually measured by averaging over a range of grains in a region ranging from micrometres to millimetres and varies continuously across the material. The micro-scale residual stress includes the Type II residual stress which arises from microstructural misfit and the Type III residual stress from the defects and dislocations induced by the welding process. Macro-scale residual stress can decrease the tensile strength of the material, while micro-scale residual stress aggravates cracking at grain level under in-service elevated temperature. Evaluating the multi-scale residual stress and microstructure, and their impact on the as-welded Eurofer97 is crucial to determining joint reliability and developing predictive tools for the in-vessel component of DEMO.

Many techniques can be used to characterise the residual stress distribution. Different approaches are appropriate for the three types of residual stress, due to technical limitations in resolution and the nature of the complex variation of microstructure, including texture, across the narrow HAZ. Multi-scale residual stress evaluation where the resolution enables the simultaneous measurement of both the macro- and micro- scale residual stress is not always possible. For examples, some attempts have been made to study the residual stress distribution in laser-welded Eurofer97 by the neutron diffraction, where the resolution is over a millimetre for macro-scale characterization (*10*, *13*). Micro-scale residual stress characterisation is therefore neglected due to low-resolution and limited precision in applying a reference stress-free lattice spacing. Digital image correlation (DIC) is one of the strain measurement techniques (*14*, *15*) that is capable of characterising average strain over a region and high-resolution (HR)- strain maps by combining with other techniques. For example, HR electron backscatter diffraction (EBSD) and DIC method is an established technique for micro-scale residual strain characterisation. However, requiring a stress-free reference is challenging, and the technique only characterises Type III residual strain (*16*, *17*). $Ga^+$ focused ion beam (FIB) and DIC method has proven reliable in measuring the time-resolved strain relaxation in titanium alloys, metallic glasses and martensitic steels (*18–20*). Although it measures residual strain without a stress-free reference two significant limitations exist which affect residual strain measurements: (i) the accelerated $Ga^+$ ions damage the material by creating defects and increasing dislocation density, which is likely to induce residual stress during the $Ga^+$ FIB milling process (*21*). (ii) to achieve a multi-scale residual stress characterisation of metallic alloys, the low removal rates of $Ga^+$ FIB usually limit the milling areas to a few micrometres, which largely achieves only Type III residual stress characterisation (*22*).

The relatively new $Xe^+$ plasma FIB (PFIB) technique gives rise to less material damage and larger volume removal within a reasonable acquisition time (*23*). Thus, the $Xe^+$ PFIB provides a potential solution for multi-scale residual stress (Types I, II&III) characterisation. Combining the $Xe^+$ PFIB with the DIC to the laser-welded Eurofer97, macro-scale residual stress can be directly measured by averaging over multiple grains within each gauge volume (i.e. milled pillar), ranging from millimetres to micrometres. Simultaneously, the micro-scale residual stress localisation in the milled pillar can be visualised by time-resolved HR strain maps.

In this study, the $Xe^+$ PFIB-DIC technique was first used to evaluate the multi-scale residual stress in laser-welded Eurofer97 steel. The macro-scale residual stress was obtained, and the time-resolved HR strain map was used to visualise the micro-scale residual strain field, which provides new insights into the initiation and propagation of creep cracking. Nanoindentation was also used to cross-validate the residual stress distribution from the $Xe^+$ PFIB-DIC technique. The micro-hardness was then evaluated for the quantitative analysis of residual stress hardening and microstructural hardening. The mechanistic connection between residual stress, microstructure and micro-hardness was established, which contributes to addressing the structural integrity for this critical engineering challenge.

## Results

### Microstructure characterisation

The methods section provides material and experimental details of Eurofer97 steel, laser conditions of welding processing and sample preparation of the laser-welded sample. The coordinates are defined in Fig. 1A, where the $x$-direction is horizontal, and the laser welding direction ($y$-) is vertical. The EBSD was used to characterise grain size and orientation distribution in the region marked by the black rectangle (4750 × 200 μm$^2$) in Fig. 1A. The grain morphology in this region, which covers the fusion zone (FZ), HAZ and base material (BM), is illustrated in Fig. 1B, made by stitching together 19 separate EBSD maps. The average grain size was extracted from EBSD orientation maps by the mean linear intercept method (*24*). The grains had an average size of 11 ± 2.10 μm in the FZ region, whereas in HAZ and BM regions, the grains show the average size of 6 ± 0.92 μm and 7 ± 1.05 μm, respectively. The stitched EBSD map shows the microstructural transition area at the centre of the FZ region and interfaces between FZ-HAZ and HAZ-BM regions. The grains in the FZ region with an obvious preferred orientation arise from the heat flow during the laser welding, which is the origin of the texture (*25*, *26*).

### Residual stress distribution characterised by $Xe^+$ plasma focused ion beam and digital image correlation (PFIB-DIC) and nanoindentation method

The $Xe^+$ PFIB-DIC technique was applied to evaluate the multi-scale residual stress of laser-welded Eurofer97. The incremental milling step using the $Xe^+$ PFIB releases residual stress gradually as the milling depth increased, and the DIC technique visualises the strain relaxation and enables residual stress measurement. The ring-core method was applied as it allows simultaneous evaluation of three components of in-plane strains relaxation ($\Delta\varepsilon_x$, $\Delta\varepsilon_y$ and $\Delta\varepsilon_{xy}$) (*27*). Fig. 1C schematically shows the ring-core incremental milling steps and SEM acquisition processes. The incremental milling was completed when the depth is equal to the ring-core diameter to avoid residual stress remaining on the pillar edge (*28*, *29*). The ring-core displacement that results from the ring-core expansion, or shrinkage, during incremental milling is recorded by the markers (the displacement between red and green markers in Fig. 1D by DIC). The strain of each marker is extracted from the gradient of the displacement. In addition, averaging of the strain of markers in the ring-core region enables measurement of the strain relaxation at each trench depth, and the 'master curve' fitting evaluates the three components of the macro-scale strain relaxation values (Fig. 1E) (*30*). The derivation of the strain relaxation in three orthogonal directions enables direct calculation of the principal strain relief using Mohr's circle (*31*). Inversion of the sign of the perceived strain relaxation provided a means of determining the residual strain, and the residual stress was then calculated using Hooke's law (*32*). The nanoindentation measurements were performed to cross-validate the residual stress distribution obtained from the $Xe^+$ PFIB-DIC ring-core method and establish the microstructural and residual stress hardening effect. As shown in Fig. 1F, the equi-biaxial residual stress was extracted by comparing the load and contact area at the same depth between residual stress and stress-free state (*33*). Performing indentation on the ring-core where the residual stress is fully released after PFIB milling provides the stress-free state and stress ratio. The location-dependent stress-free reference of FZ, HAZ and BM regions is applied to avoid differences arising from changes in microstructure during laser welding.

Performing a line scan across the weldment in the EBSD mapped regions by the $Xe^+$ PFIB-DIC ring-core method aims to establish the residual stress distribution and microstructural correlations in the FZ, HAZ and BM regions. The line-scan resolution is 200 μm in the FZ and HAZ regions and 400 μm in the BM region, as limited residual stress in the BM region is expected because of the relatively low thermal input of laser welding. The average Young's modulus and Poisson's coefficient for each ring-core in the FZ and HAZ regions were derived according to their crystallographic orientation using MTEX 5.28 on MATLAB and applied to study the anisotropic residual stress in $x$- and $y$- directions (*34–36*). It can be seen in Fig. 2A that the peaks of tensile residual stress are observed at both the FZ-HAZ and HAZ-BM interfaces, balanced by the adjacent compressive residual stresses in the HAZ region. The textured FZ regions are identified by evaluating the texture intensity of 19 separate EBSD maps using inverse pole figures (IPFs) in the $x$- and $y$- directions to enable comparison of the texture across the weldment (Fig. 2B). An example of an IPF from one of the EBSD maps that accounts for the texture intensity in multiples of random distribution (MRD) is inset in Fig. 2B. The texture is observed in the FZ region with 2.2 MRD in the $x$-direction and 4 MRD in the $y$-direction. An asymmetric residual stress profile is also identified in the high-texture FZ region, as shown in Fig. 2A. Fig. 2C illustrates the distribution of two principal residual stress components, which also exhibit peak values at the interfaces. The principal residual stress profile is also used for cross-validating the PFIB-DIC ring-core method by comparing it with the nanoindentation residual stress measurements.

Fig. 2D reveals that the residual stress distribution as measured by the nanoindentation method. The peak of compressive residual stress in the FZ is as large as –500 MPa, whereas the peak of tensile residual stress with the value up to 800 MPa occurs around the interface of FZ and HAZ regions. When moving away from the centreline of the weldment, the residual stress decreases to c. –400 MPa before reaching the BM region. Unlike the PFIB-DIC ring-core method, the nanoindentation technique has been proven to evaluate the residual stress with the assumption of equi-biaxial residual stress distribution (*33*). Compared with the residual stress distribution from the $Xe^+$ PFIB-DIC ring-core method, the profile from nanoindentation measurements shows the symmetric residual stress distribution with higher magnitudes due to the assumption of an equi-biaxial stress state.

To cross-validate the $Xe^+$ PFIB-DIC ring-core method, the equi-biaxial residual stress from nanoindentation measurement is transformed to non-equi-biaxial residual stress by employing location-dependent stress ratio ($k$) derived from the two principal residual stress components measured by the $Xe^+$ PFIB-DIC technique. The detail of this transformation can be found in the methods section. The non-equi-biaxial residual stress profile of nanoindentation measurements (Fig. 2D) displays a similar trend as the results of the $Xe^+$ PFIB-DIC technique, although the peaks of tensile residual stress in the microstructural transition areas around the FZ-HAZ and HAZ-BM interfaces show an unexpected lack of agreement regarding magnitudes (compared with Fig. 2C). This apparent discrepancy may arise due to the selection of the stress-free reference and stress ratio. The peak value of residual stress occurs at the interface of FZ-HAZ and HAZ-BM, which is consistent with the results from the $Xe^+$ PFIB-DIC ring-core method.

## Time-resolved high-resolution (HR) multi-scale strain relaxation analysis

The time-resolved strain relaxation profiles and maps were evaluated quantitatively with example ring-cores in high-texture FZ and low texture HAZ and BM regions to explore the multi-scale strain relaxation. The strain relaxation profiles (Fig. 3A, 3C and 3E) show the macro-scale strain relaxation averaged over the ring-core during the stress relief, whereas the HR strain maps (Fig. 3B, 3D and 3F) show micro-scale information at higher resolution in the ring-core. Comparing the profiles and the maps demonstrates the importance of monitoring the micro-scale strain relaxation during residual stress relief. The strain relaxation profile (Fig. 3A) presents the macro-scale strain relaxation of the ring-core in the high-texture FZ region, which shows the higher strain relaxation values of $1.2 \times 10^{-3}$ in the $x$-direction than the value of $1.05 \times 10^{-4}$ in the $y$-direction. The significant localised micro-scale strain relaxation was identified by these HR maps (Fig. 3B), where significantly higher magnitude was found in the $y$- than in the $x$-direction in the ring-core. The magnitude of localised micro-scale strain relaxation is higher than macro-scale strain relaxation profile for both examples at high-texture FZ and low texture HAZ. Significant micro-scale strain relaxation is also found in the BM regions, although the macro-scale strain relaxation is much smaller than in the FZ and HAZ regions. It also shows that micro-scale tensile strain relaxation in the region subjected to compressive strain relaxation macroscopically and vice versa. Furthermore, although the strain relaxation profiles in Fig. 3A and 3C remain stable when the value of $h/d$ reaches 0.4, the time-resolved HR strain relaxation map still captures the micro-scale strain. These findings indicate that using the time-resolved HR strain relaxation analysis enables evaluation of the micro-scale strain relaxation during the stress relief, which is neglected in the macro-scale strain relaxation profile.

## High resolution micro-scale residual strain relaxation correlated with crystal microstructures

To explore and visualise the role of micro-scale residual stress quantitatively, the displacement and HR strain relaxation of the ring-core was mapped and correlated with microstructure. Two ring-core measurements were selected from the high-texture FZ region and the low texture HAZ region to demonstrate the displacement and HR strain relaxation maps. It can be seen in Fig. 4A and Fig. 4C that the overlaid EBSD maps enable visualisation of the crystallographic orientation, and the outline (red dashed rectangle) reveals the position of the markers. The displacement maps disclose the corresponding deformation of the ring-cores due to the residual stress relief. Closer inspection of the displacement maps reveals a uniform distribution in the $x$-direction for both ring-cores and in the $y$-direction for the ring-core in the low texture HAZ region, while a linear distribution is found in the high-texture FZ region in the $y$-direction. The difference in texture intensity between these two regions is assumed to result in this linear distribution potentially. The IPF shows that the grains have a significant preferential orientation in $x$- and $y$- directions for the pillar in the high texture FZ region. This implies that the grains with different crystallographic texture show distinct deformation behavior during strain relief, resulting in the micro-scale residual stress not being in local equilibrium in the ring-core region.

By calculating the displacement gradient, the HR micro-scale strain relaxation was quantitatively evaluated and mapped. The distinct heterogeneous localised micro-scale strain relaxation was observed in both high texture FZ and low texture HAZ regions. However, due to the difference regarding grain orientation in the pillar, a layer between tensile and compressive region is found, whereas no such layer is found in the low texture HAZ region (Fig. 4C). Fig. 4B and 4D show the measured residual stress and localised texture effect schematically. In the high-texture FZ region, most grains display similar micro-scale residual stress, resulting in non-equilibrium strain relaxation during the ring-core milling. In this case, the micro-scale residual stress significantly affects the residual stress distribution. In contrast, the measured residual stress distribution in the low texture HAZ region is equivalent to the macro-scale residual stress.

## Microstructural and residual stress hardening

Local hardness values are dependent on the microstructure (e.g. grain size, the presence of martensite and precipitate size) and residual stress. The use of nanoindentation measurements enables the quantitative evaluation of the microstructural and residual stress effects on the hardness. The stress-free ring-cores provides the hardness value without the residual stress effect, where the hardness depends only on the microstructure. The measured hardness of the weldment (FZ and HAZ regions) lies in the range of 5.1 to 5.6 GPa, where the average magnitude is 5.25 ± 0.31 GPa, while this value drops to 3 ± 0.1 GPa at the HAZ-BM interface (Fig. 5A). The averaged hardness of stress-free ring-cores in the FZ and HAZ regions are shown as a dotted line and dash-dot lines, respectively, which indicates that the joined material was microstructurally hardened to 4.51 ± 0.28 GPa in the FZ region and 5.85 ± 0.33 GPa in the HAZ region by grain refinement and the presence of martensite. Looking at Fig. 5B, although the total hardening, i.e. the sum of microstructural and residual stress effects, is the same between the FZ and HAZ region, the origin of the hardening effect differs. The quantitative microstructural hardening is extracted by subtraction of the hardness of the BM from the hardness of stress-free ring-cores, which are 1.51± 0.18 GPa and 2.85 ± 0.23 GPa in the FZ and HAZ regions, respectively. Compared with the hardness of stress-free ring-cores, the quantitative residual stress effect on hardness is derived from the measured hardness, which is 0.74 ± 0.03 GPa and -0.6 ± 0.02 GPa in the FZ and HAZ regions, respectively.

## Discussion

The results demonstrate the evaluation of multi-scale residual stress distribution in the Eurofer97 weldment using $Xe^+$ PFIB-DIC ring-core methods. The residual stress distribution across the weldment is derived from the 'master curve' fitting by the $Xe^+$ PFIB-DIC ring-core method. It is worth reiterating that the asymmetric residual stress profile with sharp peaks at the interface of FZ-HAZ and HAZ-BM was observed in Fig. 2A because of the significant contribution of the non-equilibrium micro-scale residual stress to the macro-scale residual stress distribution in the weldment. The micro-scale residual stress is related to banded microstructures, texture on the surface, and regions with different microstructures. It is usually self-equilibrated over a length of around three times the grain size when there is no texture effect (*37*, *38*). However, the micro-scale residual stress is also texture dependent, which means it might become non-self-equilibrium even in a relatively large region if significant texture exists (*39*). Micro-scale residual stress can have sufficient magnitude to induce localised tensile residual stress in a region subject to compression on the macroscopic scale (*22*, *40*). During the laser welding process the local heat flow direction usually induces the texture in the weldment (*41*). The thermal gradient and associated phase transformations and solidification result in the severe microstructural misfit at the interface of FZ-HAZ and HAZ-BM. The texture in the FZ region and the microstructural misfits at the interface leads to heterogeneous mechanical properties at the microstructural level, leading to the significant mismatch between grains and micro-scale residual stress (*26*). Conventional residual stress measurements by neutron diffraction failed to capture this micro-scale residual stress in laser welded Grade91 steel. Such non-destructive residual stress measurement has a limited resolution for macro-scale measurements and usually requires a reference sample to calculate the residual stress. For example, Hughes et al. (10) performed the residual stress measurement with the constant reference *d*-spacing at the far-field region, and Kumar et al. (*42*) characterised the residual stress profile of laser-welded Grade91 steel using a comb-shaped reference sample. However, the non-equilibrium micro-scale residual stress is neglected. Given the high material removal rate of $Xe^{+}$ PFIB and HR analysis of DIC, a proper length-scale and resolution can be selected for the ring-core, allowing evaluation of macro-scale and micro-scale residual stress simultaneously, and study of the microstructural effects on heterogeneous residual stress distribution intergranular. In this project, although the texture is slightly higher (just below 4 MRD in the *y*-direction) than the low texture HAZ, the texture effect on residual stress is significant in the tens of micron length scale. As illustrated in Fig. 4B, it is assumed that the grain in similar orientation releases the micro-scale residual strain in same direction. In this case the micro-scale residual strain is not self-equilibrated in the ring-core region, which affects the residual stress distribution significantly in the high texture FZ region. In contrast, the micro- residual stress is self-equilibrated for the ring-core region in the low texture region, as shown schematically in Fig. 4D. Further evidence is found in the low texture BM region where significant micro-scale residual stress is observed, but the macro-scale strain relaxation is not evident (Fig. 3E and 3F).

Here, the residual stress distribution was also measured using a nanoindentation method by averaging over five line-scans. The nanoindentation residual stress measurement is performed with the assumption of equi-biaxial residual stress distribution in the weldments. As shown in Fig. 2D, the equi-biaxial residual stress ($\sigma_{equi}^{indent}$) presents the generally symmetric 'M-shape' residual stress distribution, which is consistent with the neutron diffraction residual stress measurement on the laser-welded Grade91 steel (*42*). Lee *et al*. proposed a stress ratio to extract the two principal residual stress components in an arbitrary non-equi-biaxial state from the average equi-biaxial residual stress (*43*). Until now, only a constant stress ratio of 0.33 could be applied to achieve the non-equi-biaxial residual stress evaluation on the weldment (*44*). Use of the $Xe^{+}$ PFIB-DIC ring-core method provides the location-dependent stress ratio (*k*) to transfer the equi-biaxial residual stress to non-equi-biaxial to overcome the primary limitation of nanoindentation residual stress measurement and cross-validate the two techniques. The two principal residual stress components from nanoindentation measurements ($\sigma_1^{indent}$ and $\sigma_2^{indent}$) in the Fig. 2D, show a similar trend to that of the ring-core method (Fig. 2A). However, some unexpected inconsistency occurs at the position where the non-equilibrium micro-scale residual stress exists, e.g. high-texture FZ region and microstructural transition areas. This reveals the limitation of nanoindentation residual stress measurement, with its intrinsic difficulty of selecting a truly stress-free reference and stress ratio for non-equi-biaxial residual stress calculation in complex material systems. On the one hand, the sharp microstructure and residual stress gradients usually exists in these transition regions, which implies that the location-dependent stress-free reference at high resolution is desirable to improve the quality of the nanoindentation residual stress measurements. On the other hand, the stress ratio in the high-texture FZ region consists of macro-scale and non-equilibrium micro-scale residual stresses, which is unable to provide the accurate stress ratio for non-equi-biaxial residual stress evaluation. Further work is needed to optimise the location-dependent stress-free reference and macro-scale stress ratio at the narrow transition areas to develop the next generation of advanced nanoindentation residual stress measurement, leading to more accurate measurement with reduced uncertainty.

Additionally, combining the two techniques enables the quantitative analysis of the microstructural and macro-scale residual stress hardening (Fig. 5A and 5B), enabling evaluation of the underpinning mechanisms of degradation of mechanical property of the laser-welded weldment. Microstructural hardening is the result of the presence of precipitates, grain boundary strengthening and the martensite transformation in the FZ and HAZ regions (*45–47*). The compressive residual stress aggravates the hardening phenomenon in the FZ region, while the tensile residual stress softens the material in the HAZ. Both methods enabled consideration of the macro-scale biaxial residual stress, achieving an improved understanding of residual stress distribution in the weldment.

As the $Xe^+$ PFIB-DIC technique does not require a reference, this technique provides a more reliable residual stress distribution in the transition areas.

The $Xe^+$ PFIB-DIC technique can also map time-resolved HR micro-scale strain relaxation, which provides insight into analysing the void formation and creep cracking caused by residual stress relief. It has been widely reported that the creep cracks are a significant challenge for Grade91 steel under load at high temperature and residual stress is often considered as the most primary reason for creep cracking (*48*, *49*). The high operating temperature triggers the thermal relaxation of welding-induced residual stress. The accumulation of micro-scale strain relaxation during the thermal residual stress relief leads to the formation of the voids and creep crack initiation (*50–52*). Such accumulation during the residual stress relaxation can be visualised by the time-resolved HR strain relaxation maps. It can be seen in Fig. 3 that even in the region that is subject to compressive macro-scale strain that the micro-scale residual strain is sufficient to form tensile localised residual strain. The use of time-resolved HR strain maps is valuable for identifying and quantifying sharp micro-scale strain relaxation gradients and strain accumulation during residual stress relief. It provides critical information necessary for developing a micromechanical rationale for failure. The $Xe^+$ PFIB-DIC technique, however, has some limitations that require careful consideration. Due to the SEM's serial acquisition the pixels in *x*-, *xy*- and *y*- directions are in order of increasing scanning time gap (*19*), this results in the broadening of the range of the 95% confidence interval in *xy*- and *y*- directions compared to the *x*-direction. Additionally, although the Type I, II and III strain relaxations are identified based on their locations, further work is still necessary to quantitatively characterise the magnitude of Type I, II and III residual stresses on the time-resolved HR strain relaxation maps.

In conclusion, our analysis of the heterogeneous microstructural and residual stress distribution in laser-welded Eufofer97 steel, through the combination of EBSD, $Xe^+$ PFIB-DIC and nanoindentation, offers new tools for evaluating multi-scale residual stress and providing new insight into the critical engineering challenges of laser welded Eurofer97 steel and other complex weldments. With the $Xe^+$ PFIB-DIC ring-core method the macro-scale residual stress is characterised across the weldment, and the micro-scale residual stress is observed from time-resolved HR strain relaxation maps. The non-equilibrium micro-scale residual stress in high texture regions significantly affects the macro-scale residual stress, rationalising the asymmetric residual stress distribution. The time-resolved HR- strain relaxation map was first used to visualise the micro-scale residual strain field -- the precursor of void formation and crack initiation during residual stress relief. The mechanistic connection between residual stress, microstructure and micro-hardness is established, where the residual stress contributes around 25 % to hardening and softening in the FZ and HAZ, respectively. Further analysis enables extraction of a coefficient using the $Xe^+$ PFIB-DIC technique. This method enables the reconstruction of the residual stress from equi-biaxial to non-equi-biaxial by considering texture effects. This has great potential to overcome the current limitation of nanoindentation residual stress measurement. The $Xe^+$ PFIB-DIC ring-core method is now available for the evaluation of HR multi-scale residual stress heterogeneity in welded in-vessel fusion components or even more complex material system.

## Materials and Methods

### Materials

The as-received 6mm thick Eurofer97 steel (made by Böhler Austria GmbH) had a composition Fe-0.11C-8.82Cr-1.08W-0.13Ta-0.48Mn-0.2V (in wt.%). Reith et al. have described the detailed fabrication and heat treatment of as-received Eurofer97 steel in a previous study (*46*). The Eurofer97 plate butt-weld was made from two plates, each $150 \times 75 \times 6$ $mm^3$. The single-pass laser weld was made using a Yb-fibre laser source with a spot size of 200 μm and a welding speed of 1.2

m/min at TWI to attain a high-quality weld (narrow penetrating bead and slightly concave. As shown in Fig. 1A the as-welded sample used in this research was cut from the as-welded Eurofer97 plate by electrical discharge machining, and the size was ~25 × 6 × 6 $mm^3$.

The microstructure was characterised using a Jeol-7100F SEM, equipped with a Thermo Fisher Lumis EBSD detector. Suitable sample preparation processes were applied in a sequence of mechanical polishing, vibration polishing using 0.3 μm colloidal silica and etching with Vilella's reagent (1 g picric, 5 ml HCL and 100 ml ethanol). The 19 EBSD maps were captured with a resolution of 512 × 384 pixels using an accelerating voltage of 20 kV and beam current of 12 nA with a step size of 0.6 μm and a 2 × 2 pattern binning. Pathfinder$^{TM}$ software was used to collect the EBSD orientation data, and MTEX 5.2.8 software was applied to analyse the crystallographic orientation, calculate the texture intensity, average Young's modulus and Poisson's ratio. The post-processing of the raw EBSD orientation data began with filtering, which filled the missing data using the interpolation method of the nearest neighbour. Denoising was then performed according to the deviations from the true orientation. The grains were reconstructed by reducing the orientation noise with a lower threshold of 15 °. The grain morphology in the region of 4750 × 200 $\mu m^2$ (dashed rectangle in Fig. 1A), which covers FZ, HAZ and BM, were visualised by stitching the 19 separate EBSD maps. The IPF characterised the texture of each EBSD map in both *x*- and *y*-directions (representative IPF in Fig. 2B) by the texture intensity. The highest intensity in the IPF of each separate EBSD mapping was employed to describe the distribution of texture circumstances across the weldment in *x*- and *y*- directions. The average Young's modulus and Poisson's coefficient were evaluated from elastic constants of as-received Eurofer97 according to the crystallographic orientation.

## $Xe^+$ PFIB-DIC ring-core method

The Xe+ PFIB-DIC ring-core method comprises two procedures: SEM image acquisition during incremental PFIB milling (Fig. 1C) and residual stress measurement (Fig. 1D-E). The first procedure was performed using a Tescan MIRA 3 PFIB-SEM. Given the different grain size at different regions, the inner diameter of the ring-core (d) of 30 μm at the FZ region and 20 μm at the HAZ and BM regions enabled sufficient grains to be captured within a reasonable data acquisition time. The final milling depth (*h*) was equal to the inner diameter to avoid any remaining residual stress at the ring-core edge, and a uniform milling depth was used for each incremental step. Fifty milling steps were performed at a beam energy of 30 keV and beam current of 15 nA, which achieved full relief of residual stress (i.e. when $h/d = 1$). Ten secondary electron (SE) images were acquired with a spot size of 10 nm in every incremental step to record the strain relaxation. The processes of incremental milling and SE image acquisition were performed with the help of a specifically developed automated programme by TESCAN s.r.o.

Customised MATLAB-based DIC software was employed to perform strain relaxation correlation (*53*). The first step of DIC was the correlation analysis over the stack of SE images. A Gaussian filter was used to denoise the raw SEM images, and a fiducial mesh was used to track the ring-core deformation of the central region to avoid the stress concentration at the pillar edge. The fiducial mesh in the space of 20 pixels (200 nm) were used as the 'subset' to record ring-core displacements in high resolution (Fig. 1D). The pre-set 'subset' used for tracking a single node movement was 31 × 31 pixels, which ensured that single node movement occurred only in the subset region with a minimum of boundary effects (*54*). The outline shape of the mesh is highlighted in Fig. 4A and Fig. 4C, representing the deformation of the ring-core. The correlation results for 10 SE images in the same incremental milling step were averaged to reduce noise. The outliers (poorly tracked nodes) were removed in post-processing to estimate ring-core displacements in high accuracy and precision. The detail of the outlier removal process has been reported previously (*55*). The HR ring-core displacements were analysed by tracking the node movements, as shown in Fig. 4A and Fig. 4C. The gradient of the single node movement was evaluated to quantify the ring-core strain relaxation. To visualise time-resolved HR strain relaxation maps, the strain values of each node were converted into a colour-coded map for each incremental milling step, achieving the resolution of 200 × 200 nm$^2$.

Finally, the linear fit to all node movements, with their fiducial position, yielded time-resolved strain relaxation for each incremental milling step using the least-squares function. The time-resolved strain relaxation was fitted to the 'master curve' function to obtain the full in-plane strain relaxation components accompanied by the error bars that correspond to a 95% confidence level (*30*). The residual stress was then calculated by Hooke's law, where the out of plane stress is negligible (*32*):

$$\sigma_x^{PFIB} = -\frac{E_{avg}}{(1-v_{avg}^2)}\left[\Delta\varepsilon_\infty^{x} + v\Delta\varepsilon_\infty^{y}\right] \qquad \textit{Eq. 1}$$

$$\sigma_y^{PFIB} = -\frac{E_{avg}}{(1-v_{avg}^2)}\left[\Delta\varepsilon_\infty^{y} + v\Delta\varepsilon_\infty^{x}\right] \qquad \textit{Eq. 2}$$

where $\Delta\varepsilon_\infty^{x}$ and $\Delta\varepsilon_\infty^{y}$ are the strain relaxations and $\sigma_x$ and $\sigma_y$ are two in-plane residual stress components in the *x*- and *y*- directions. $E_{avg}$ and $v_{avg}$ are average Young's modulus and Poisson's coefficients of the region where the ring-core located.

## Nanoindentation

The nanoindentation measurement was carried out using an Agilent G200 nano indenter with a Berkovich indenter tip at the UKAEA's Materials Research Facility. Strain rate-controlled indentations were carried out to 1.5 µm depth using continuous stiffness mode (2 nm amplitude, 45 Hz frequency, 0.05/s strain rate), and the mechanical properties were determined according to the theory by Oliver and Pharr (*56*). An array of 5 × 40 indentations was performed on the as-welded sample, see Fig. 1A. The nanoindentation measurements in the *x*-direction were in the space of 200 µm, while the interval between nanoindentation in a column in the *y*-direction was 30 µm. Since the ring-core is considered notionally stress-free, the location-dependent stress-free nanoindentation tests were carried out on the ring-cores at the FZ, HAZ and BM regions. The setup for executing a stress-free nanoindentation test was the same as performing a nanoindentation array-scan. To avoid error due to insufficient stiffness of the reference ring-core, the hardness values reported are an average of the depth-resolved hardness from 100 to 500 nm deep, and the load and contact area were extracted for a depth of 500 nm for residual stress evaluation. The residual stress from nanoindentation measurement ($\sigma_{equi}^{indent}$) is assumed to be equi-biaxial and uniform in the near-surface region in this technique (*57*, *58*). The method of deriving the residual stress from comparing the difference regarding load-depth curves and contact areas between residual stress and stress-free states has been discussed elsewhere (*33*, *58*). To cross-validate the results from the PFIB-DIC technique, the equi-biaxial residual stress ($\sigma_{equi}^{indent}$) was transformed to the non-equi-biaxial residual stress (major and minor principal stress $\sigma_1^{indent}$ and $\sigma_2^{indent}$) via the location-dependent stress ratio k at corresponding position in the following manner:

$$k = \frac{\sigma_1^{PFIB}}{\sigma_2^{PFIB}}\ (-1 < k < 1\ and\ k\ \neq 0) \qquad \textit{Eq. 3}$$

$$\sigma_1^{indent} = \frac{3(L_0-L)}{(1+k)A_C} \qquad \textit{Eq. 4}$$

$$\sigma_2^{indent} = k\sigma_1^{indent} = \frac{3k(L_0-L)}{(1+k)A_C} \qquad \textit{Eq. 5}$$

where the $\sigma_1^{PFIB}$ and $\sigma_2^{PFIB}$ are the major and minor principal residual stress components from the PFIB-DIC ring-core method, respectively.

## References


1. R. Lässer, N. Baluc, J. L. Boutard, E. Diegele, S. Dudarev, M. Gasparotto, A. Möslang, R. Pippan, B. Riccardi, B. van der Schaaf, Structural materials for DEMO: The EU development, strategy, testing and modelling. *Fusion Eng. Des.* **82**, 511–520 (2007).
2. R. Andreani, E. Diegele, R. Laesser, B. Van Der Schaaf, in *Journal of Nuclear Materials* (North-Holland, 2004), vols. 329–333, pp. 20–30.
3. S. Kirk, W. Suder, K. Keogh, T. Tremethick, A. Loving, Laser welding of fusion relevant steels for the European DEMO. *Fusion Eng. Des.* (2018), doi:10.1016/j.fusengdes.2018.03.039.
4. P. Aubert, F. Tavassoli, M. Rieth, E. Diegele, Y. Poitevin, Low activation steels welding with PWHT and coating for ITER test blanket modules and DEMO. *J. Nucl. Mater.* **409**, 156–162 (2011).
5. H. Tanigawa, T. Maruyama, Y. Noguchi, N. Takeda, S. Kakudate, Laser welding to expand the allowable gap in bore welding for ITER blanket hydraulic connection. *Fusion Eng. Des.* **98–99**, 1634–1637 (2015).
6. P. Aubert, F. Tavassoli, M. Rieth, E. Diegele, Y. Poitevin, Review of candidate welding processes of RAFM steels for ITER test blanket modules and DEMO. *J. Nucl. Mater.* **417**, 43–50 (2011).
7. P. Fernández, A. . Lancha, J. Lapeña, M. Serrano, M. Hernández-Mayoral, Metallurgical properties of reduced activation martensitic steel Eurofer'97 in the as-received condition and after thermal ageing. *J. Nucl. Mater.* **307–311**, 495–499 (2002).
8. X. Li, X. Li, S. Schönecker, R. Li, J. Zhao, L. Vitos, Understanding the mechanical properties of reduced activation steels. *Mater. Des.* **146**, 260–272 (2018).
9. M. Rieth, M. Schirra, A. Falkenstein, P. Graf, S. Heger, H. Kempe, R. Lindau, H. Zimmermann, EUROFER 97 Tensile, charpy, creep and structural tests, 68 (2003).
10. D. J. Hughes, E. Koukovini-Platia, E. L. Heeley, Residual stress in a laser welded EUROFER blanket module assembly using non-destructive neutron diffraction techniques. *Fusion Eng. Des.* **89**, 104–108 (2014).
11. S. Kumar, A. Kundu, K. A. Venkata, A. Evans, C. E. Truman, J. A. Francis, K. Bhanumurthy, P. J. Bouchard, G. K. Dey, Residual stresses in laser welded ASTM A387 Grade 91 steel plates. *Mater. Sci. Eng. A*. **575**, 160–168 (2013).
12. P. J. J. Withers, H. K. D. H. K. D. H. Bhadeshia, Residual stress. Part 1 – Measurement techniques. *Mater. Sci. Technol.* **17**, 355–365 (2013).
13. R. Coppola, O. Asserin, P. Aubert, C. Braham, A. Monnier, M. Valli, E. Diegele, Characterization of residual stresses in Eurofer welded specimens: Measurements by neutron diffraction and comparison with weld modeling. *J. Nucl. Mater.* **417**, 51–54 (2011).
14. D. J. Shiwarski, J. W. Tashman, A. Tsamis, J. M. Bliley, M. A. Blundon, E. Aranda-Michel, Q. Jallerat, J. M. Szymanski, B. M. McCartney, A. W. Feinberg, Fibronectin-based nanomechanical biosensors to map 3D surface strains in live cells and tissue. *Nat. Commun.* **11**, 5883 (2020).
15. Y. Xu, S. Joseph, P. Karamched, K. Fox, D. Rugg, F. P. E. Dunne, D. Dye, Predicting dwell fatigue life in titanium alloys using modelling and experiment. *Nat. Commun.* **11**, 5868 (2020).
16. J. Jiang, T. B. Britton, A. J. Wilkinson, Mapping type III intragranular residual stress distributions in deformed copper polycrystals. *Acta Mater.* **61**, 5895–5904 (2013).
17. C. Yildirim, C. Jessop, J. Ahlström, C. Detlefs, Y. Zhang, 3D mapping of orientation

variation and local residual stress within individual grains of pearlitic steel using synchrotron dark field X-ray microscopy. *Scr. Mater.* **197**, 113783 (2021).
18. J. Everaerts, E. Salvati, F. Uzun, L. Romano Brandt, H. Zhang, A. M. Korsunsky, Separating macro- (Type I) and micro- (Type II+III) residual stresses by ring-core FIB-DIC milling and eigenstrain modelling of a plastically bent titanium alloy bar. *Acta Mater.* **156**, 43–51 (2018).
19. F. Archie, M. Z. Mughal, M. Sebastiani, E. Bemporad, S. Zaefferer, Anisotropic distribution of the micro residual stresses in lath martensite revealed by FIB ring-core milling technique. *Acta Mater.* **150**, 327–338 (2018).
20. S. Haratian, F. Niessen, F. B. Grumsen, M. J. B. Nancarrow, E. V. Pereloma, M. Villa, T. L. Christiansen, M. A. J. Somers, Strain, stress and stress relaxation in oxidized ZrCuAl-based bulk metallic glass. *Acta Mater.* **200**, 674–685 (2020).
21. Y. Xiao, J. Wehrs, H. Ma, T. Al-Samman, S. Korte-Kerzel, M. Göken, J. Michler, R. Spolenak, J. M. Wheeler, Investigation of the deformation behavior of aluminum micropillars produced by focused ion beam machining using Ga and Xe ions. *Scr. Mater.* **127**, 191–194 (2017).
22. J. Everaerts, X. Song, B. Nagarajan, A. M. Korsunsky, Evaluation of macro- and microscopic residual stresses in laser shock-peened titanium alloy by FIB-DIC ring-core milling with different core diameters. *Surf. Coatings Technol.* **349**, 719–724 (2018).
23. T. L. Burnett, R. Kelley, B. Winiarski, L. Contreras, M. Daly, A. Gholinia, M. G. Burke, P. J. Withers, Large volume serial section tomography by Xe Plasma FIB dual beam microscopy. *Ultramicroscopy*. **161**, 119–129 (2016).
24. B. Roebuck, E. G. Bennett, A. Dickson, “The measurement of uncertainty in grain size distribution. Interlaboratory exercise part 1-reference images” (National Physical Lab., 1999).
25. R. S. Coelho, A. Kostka, H. Pinto, S. Riekehr, M. Koçak, A. R. Pyzalla, Microstructure and mechanical properties of magnesium alloy AZ31B laser beam welds. *Mater. Sci. Eng. A*. **485**, 20–30 (2008).
26. W. Woo, H. Choo, M. B. Prime, Z. Feng, B. Clausen, Microstructure, texture and residual stress in a friction-stir-processed AZ31B magnesium alloy. *Acta Mater.* **56**, 1701–1711 (2008).
27. E. Salvati, T. Sui, A. M. Korsunsky, Uncertainty quantification of residual stress evaluation by the FIB-DIC ring-core method due to elastic anisotropy effects. *Int. J. Solids Struct.* **87**, 61–69 (2016).
28. J. Lord, D. Cox, A. Ratzke, M. Sebastiani, A. Korsunsky, E. Salvati, M. Z. Mughal, E. Bemporad, A good practice guide for measuring residual stresses using FIB-DIC (2018).
29. A. M. Korsunsky, E. Salvati, A. G. J. J. Lunt, T. Sui, M. Z. Mughal, R. Daniel, J. Keckes, E. Bemporad, M. Sebastiani, Nanoscale residual stress depth profiling by Focused Ion Beam milling and eigenstrain analysis. *Mater. Des.* **145**, 55–64 (2018).
30. A. M. Korsunsky, M. Sebastiani, E. Bemporad, Residual stress evaluation at the micrometer scale: Analysis of thin coatings by FIB milling and digital image correlation. *Surf. Coatings Technol.* **205**, 2393–2403 (2010).
31. A. J. G. G. Lunt, A. M. Korsunsky, A review of micro-scale focused ion beam milling and digital image correlation analysis for residual stress evaluation and error estimation. *Surf. Coatings Technol.* **283** (2015), pp. 373–388.
32. A. M. Korsunsky, M. Sebastiani, E. Bemporad, Focused ion beam ring drilling for residual stress evaluation. *Mater. Lett.* **63**, 1961–1963 (2009).
33. Y. H. Lee, D. Kwon, Measurement of residual-stress effect by nanoindentation on elastically strained (1 0 0) W. *Scr. Mater.* **49**, 459–465 (2003).
34. F. Bachmann, R. Hielscher, H. Schaeben, in *Solid State Phenomena* (Trans Tech Publ,

2010), vol. 160, pp. 63–68.
35. D. Mainprice, F. Bachmann, R. Hielscher, H. Schaeben, G. E. Lloyd, Calculating anisotropic piezoelectric properties from texture data using the MTEX open source package. *Geol. Soc. Spec. Publ.* **409**, 223–249 (2015).
36. D. Mainprice, R. Hielscher, H. Schaeben, Calculating anisotropic physical properties from texture data using the MTEX open-source package. *Geol. Soc. Spec. Publ.* **360**, 175–192 (2011).
37. G. Van Boven, W. Chen, R. Rogge, The role of residual stress in neutral pH stress corrosion cracking of pipeline steels. Part I: Pitting and cracking occurrence. *Acta Mater.* **55**, 29–42 (2007).
38. P. J. Withers, H. K. D. H. Bhadeshia, Residual stress. Part 2 – Nature and origins. *Mater. Sci. Technol.* **17**, 366–375 (2013).
39. Y. D. Wang, R. Lin Peng, X.-L. Wang, R. L. McGreevy, Grain-orientation-dependent residual stress and the effect of annealing in cold-rolled stainless steel. *Acta Mater.* **50**, 1717–1734 (2002).
40. E. Salvati, A. M. Korsunsky, An analysis of macro- and micro-scale residual stresses of Type I, II and III using FIB-DIC micro-ring-core milling and crystal plasticity FE modelling. *Int. J. Plast.* **98**, 123–138 (2017).
41. H. L. Wei, J. Mazumder, T. DebRoy, Evolution of solidification texture during additive manufacturing. *Sci. Rep.* **5**, 1–7 (2015).
42. S. Kumar, A. Kundu, K. A. Venkata, A. Evans, C. E. Truman, J. A. Francis, K. Bhanumurthy, P. J. Bouchard, G. K. Dey, Residual stresses in laser welded ASTM A387 Grade 91 steel plates. *Mater. Sci. Eng. A*. **575**, 160–168 (2013).
43. Y. H. Lee, D. Kwon, Estimation of biaxial surface stress by instrumented indentation with sharp indenters. *Acta Mater.* **52**, 1555–1563 (2004).
44. Y. Lee, J. Y. Kim, J. S. Lee, K. H. Kim, J. Y. Koo, D. Kwon, in *Philosophical Magazine* (2006), vol. 86, pp. 5497–5504.
45. P. Aubert, F. Tavassoli, M. Rieth, E. Diegele, Y. Poitevin, Low activation steels welding with PWHT and coating for ITER test blanket modules and DEMO. *J. Nucl. Mater.* **409**, 156–162 (2011).
46. M. Rieth, M. Schirra, A. Falkenstein, P. Graf, S. Heger, H. Kempe, R. Lindau, H. Zimmermann, “EUROFER 97 Tensile, charpy, creep and structural tests” (Germany, 2003), (available at http://inis.iaea.org/search/search.aspx?orig_q=RN:35032617).
47. M. Klimenkov, R. Lindau, E. Materna-Morris, A. Möslang, in *Progress in Nuclear Energy* (Pergamon, 2012), vol. 57, pp. 8–13.
48. Y. Wang, R. Kannan, L. Li, Insight into Type IV cracking in Grade 91 steel weldments. *Mater. Des.* **190**, 108570 (2020).
49. M. Turski, P. J. Bouchard, A. Steuwer, P. J. Withers, Residual stress driven creep cracking in AISI Type 316 stainless steel. *Acta Mater.* **56**, 3598–3612 (2008).
50. H. Fu, B. Dönges, U. Krupp, U. Pietsch, C. P. Fritzen, X. Yun, H. J. Christ, Microcrack initiation mechanism of a duplex stainless steel under very high cycle fatigue loading condition: The significance of load partitioning and micro residual stresses. *Acta Mater.* **199**, 278–287 (2020).
51. P. J. Bouchard, P. J. Withers, S. A. McDonald, R. K. Heenan, Quantification of creep cavitation damage around a crack in a stainless steel pressure vessel. *Acta Mater.* **52**, 23–34 (2004).
52. T. Shrestha, M. Basirat, S. Alsagabi, A. Sittiho, I. Charit, G. P. Potirniche, Creep rupture behavior of welded Grade 91 steel. *Mater. Sci. Eng. A*. **669**, 75–86 (2016).
53. Digital Image Correlation and Tracking - File Exchange - MATLAB Central, (available at https://uk.mathworks.com/matlabcentral/fileexchange/50994-digital-image-correlation-

and-tracking).
54. H. Zhang, M. Senn, T. Sui, A. J. G. Lunt, L. Brandt, C. Papadaki, S. Ying, E. Salvati, C. Eberl, A. Korsunsky, in *WCE 2017* (2017).
55. A. J. G. Lunt, A. M. Korsunsky, A review of micro-scale focused ion beam milling and digital image correlation analysis for residual stress evaluation and error estimation. *Surf. Coatings Technol.* **283** (2015), pp. 373–388.
56. G. M. Pharr, An improved technique for determining hardness and elastic modulus using load and displacement sensing indentation experiments. *J. Mater. Res.* **7**, 1564–1583 (1992).
57. M. K. Khan, M. E. Fitzpatrick, S. V Hainsworth, A. D. Evans, L. Edwards, Application of synchrotron X-ray diffraction and nanoindentation for the determination of residual stress fields around scratches. *Acta Mater.* **59**, 7508–7520 (2011).
58. C. A. Charitidis, D. A. Dragatogiannis, E. P. Koumoulos, I. A. Kartsonakis, Residual stress and deformation mechanism of friction stir welded aluminum alloys by nanoindentation. *Mater. Sci. Eng. A*. **540**, 226–234 (2012).

## Acknowledgements

The authors give thanks to the Karlsruhe Institute for Technology for providing the Eurofer97 plate for this study and Dr Simon Kirk (UKAEA) for his advice on laser welding. The authors would like to thank Dr David Cox and Mr David Jones, from the University of Surrey, for their support and assistance during the sample preparation, experiment and data analysis. The Doctoral College Studentship Award 2 (DCSA2) of the University of Surrey is acknowledged for the funding support. This work has been carried out within the framework of the EUROfusion Consortium and has received (part) funding from the Euratom Research and Training Programme 2014 - 2018 and 2019 - 2020 under grant agreement No 633053. The views and options expressed herein do not necessarily reflect those of the European Commission. The research used UKAEA's Materials Research Facility, which has been funded by and is part of the UK's National Nuclear User Facility and Henry Royce Institute for Advanced Materials. Dr Wang, Dr London and Dr Gorley would also like to acknowledge the RCUK Energy Programme [grant EP/T012250/1] and the UK Government Department for Business, Energy and Industrial Strategy for time and resources.

## Author Contributions

Conceptualisation: Tan Sui
Methodology: Tan Sui, Jiří Dluhoš, Andrew J. London
Investigation: Bin Zhu
Supervision: Tan Sui, Mark Whiting, Yiqiang Wang, Michael Gorley
Writing—original draft: Bin Zhu
Writing—review & editing: all authors

All other authors declare they have no competing interests.

## Figures and Tables

**Fig. 1. Experimental schematic illustration and microstructural characterisation. (A)** Schematic figure showing the areas and positions of EBSD mapping, nanoindentation and PFIB-DIC. (**B)** Stitching map showing the grain size, shape and orientation. (**C)** Schematic figure illustrating SEM image acquisition during $Xe^+$ PFIB incremental milling steps. (**D)** Illustration of the tracking of the ring-core, using the displacement between fiducial mesh and the mesh after

milling increments. **(E)** Strain relaxation profiles at incremental normalised trench depth (*h/d*) and master fitting curve along *x*-, *y*- and *xy*- directions, and the error bar shows the 95% confidence interval. **(F)** Schematic figure of residual stress measurement by nanoindentation and an example of location-dependent stress-free reference.

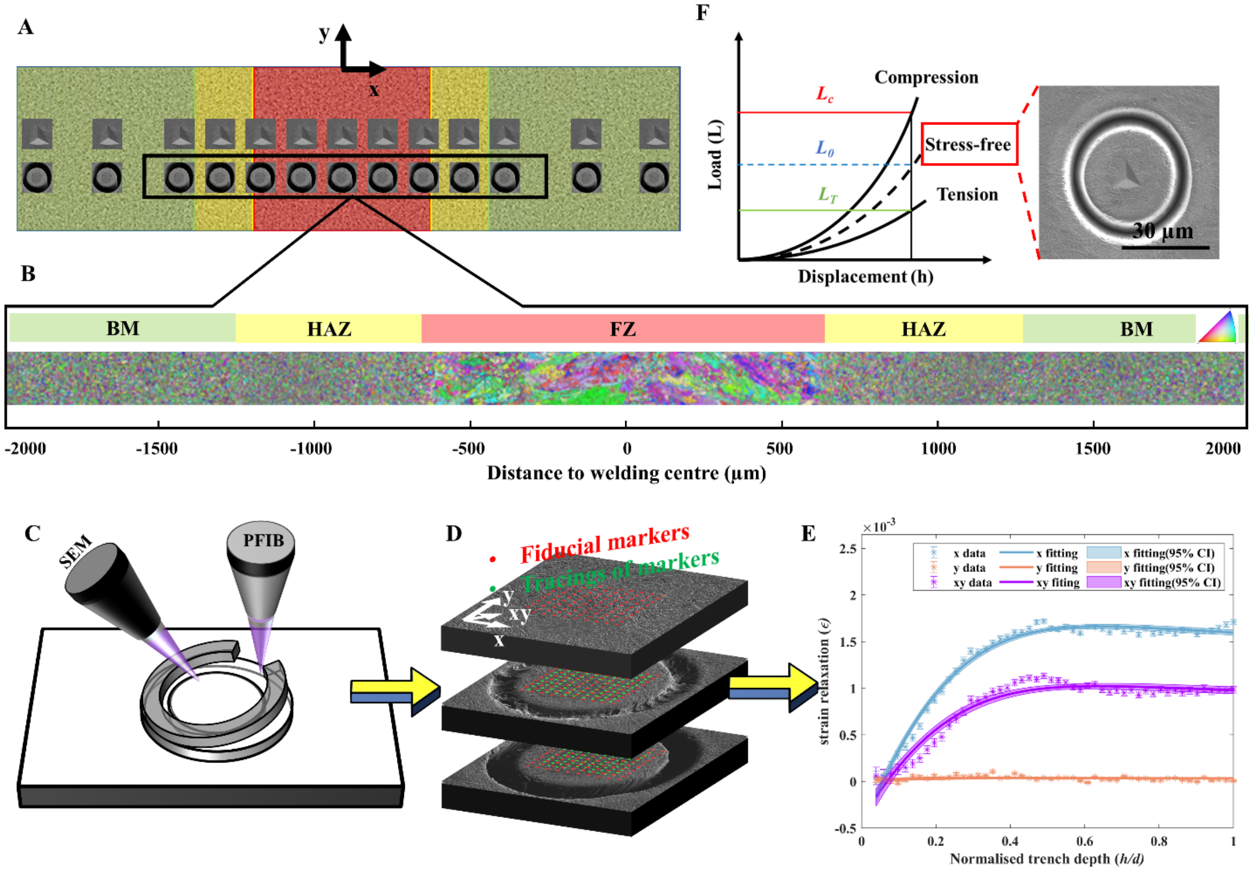

**Fig. 2. Residual stress distribution across the weldment. (A)** Residual stress distribution in $x$- and $y$- directions measured by $Xe^+$ PFIB-DIC ring-core method. **(B)** Texture distribution across the weldment in $x$- and $y$- directions, and the example IPF in the FZ region. **(C)** Principal residual stress distribution across the weldment from $Xe^+$ PFIB-DIC ring-core method. **(D)** Equi-biaxial and non-equi-biaxial residual stress distribution measured by nanoindentation residual stress measurement.

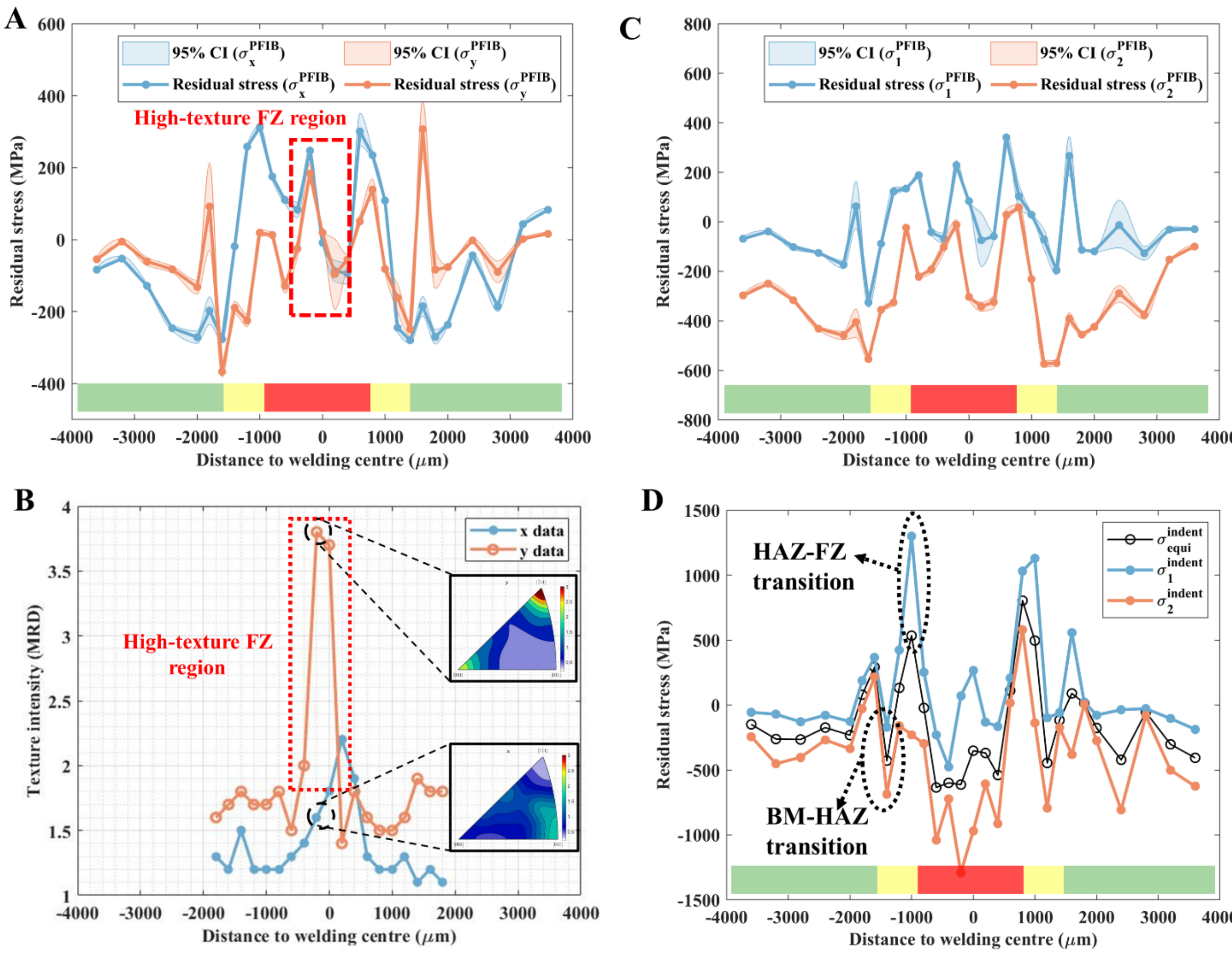

**Fig. 3. The time-resolved multi-scale strain relaxation during $Xe^+$ PFIB milling step. (A)** Strain relaxation profile of the ring-core at high-texture FZ region in the *x*- and *y*- directions with 95% CI. **(B)** Corresponding time-resolved HR strain relaxation maps in the *x*- and *y*- directions. (**C**) Strain relaxation profile of the ring-core at low texture HAZ region in the *x*- and *y*- directions with 95% CI. **(D)** Corresponding time-resolved HR strain relaxation maps in the *x*- and *y*- directions. (**E**) Strain relaxation profile of the ring-core at low texture HAZ region in the *x*- and *y*- directions with 95% CI. **(F)** Corresponding time-resolved HR strain relaxation maps in the *x*- and *y*- directions.

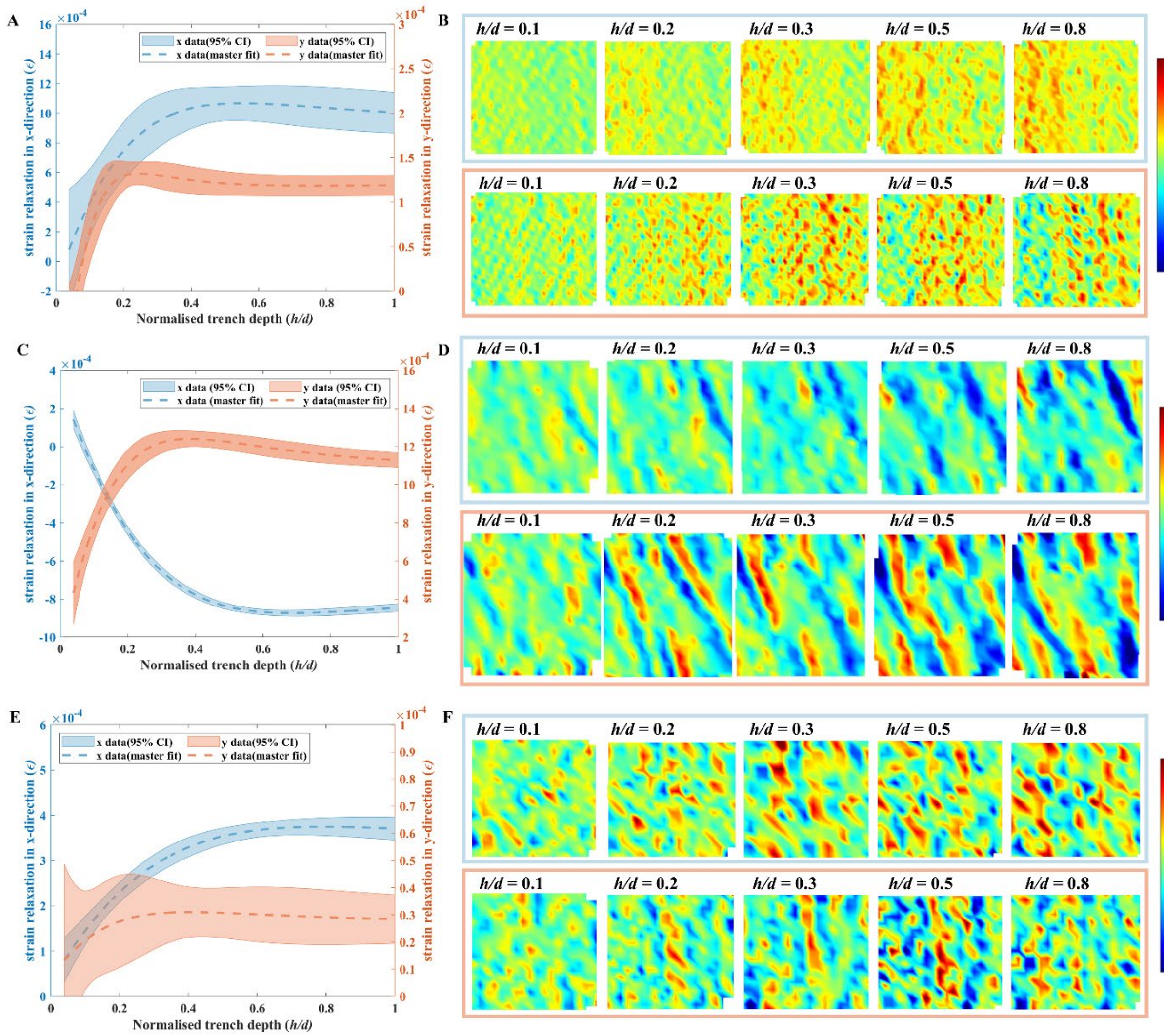

**Fig. 4. Examples of displacement and strain relaxation mapping in the high-texture FZ and low texture HAZ regions. (A)** and **(C)** The texture intensity and the crystallographic orientation of the ring-cores and the outline of the fiducial marker array (red rectangle). The displacement maps of the ring-core and the HR strain relaxation maps overlaid by the grain boundary in $x$- and $y$-directions indicate the strain partitioning and strain relaxation localisation. **(B)** and **(D)** Schematically figures explain the texture effects on residual stress evaluation by the PFIB-DIC ring-core method.

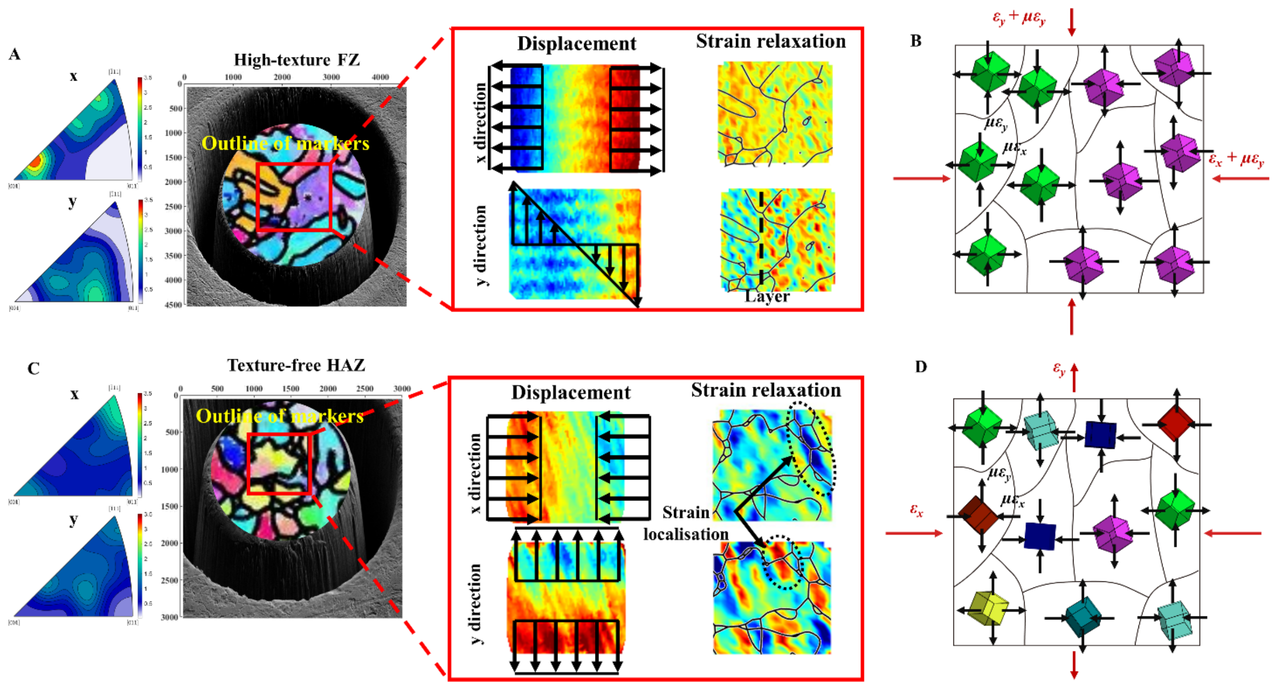

**Fig. 5. Residual stress measurements using the nanoindentation, and residual stress and microstructural effects on micro-hardness. (A)** The micro-hardness distribution across the joint and the average micro-hardness of the stress-free ring-cores in FZ and HAZ regions. (**B)** Quantitative analysis of residual stress and microstructural hardening/softening in the FZ and HAZ regions.